


***Ab initio* constraints on the melting of silica at high pressures up to 500 GPa**Ming Geng (耿明) <sup>1,2</sup> and Chris E. Mohn<sup>1,2,3,\*</sup><sup>1</sup>*Centre for Earth Evolution and Dynamics, University of Oslo, N-0315 Oslo, Norway*<sup>2</sup>*Centre for Planetary Habitability, University of Oslo, N-0315 Oslo, Norway*<sup>3</sup>*Department of Chemistry and Center for Materials Science and Nanotechnology, University of Oslo, Oslo 0371, Norway*

(Received 10 July 2023; revised 18 November 2023; accepted 15 December 2023; published 18 January 2024)

The melting curve of pure silica (SiO<sub>2</sub>) was determined using *ab initio* density functional theory together with the solid-liquid coexisting approach, thermodynamic integration, and the Z method. The melting curves are consistent with a smooth, slow increase in a large region from 50 GPa ( $dT/dP \approx 15$  K/GPa) to about 500 GPa ( $dT/dP \approx 5$  K/GPa) without any abrupt changes at around 120 and 300 GPa as seen in some recent experimental and computational studies. The topography of the melting curve above 50 GPa is consistent with a gradual change in the distribution of the Si coordination numbers in the liquid state and the absence of large changes in the density following solid-solid phase transitions. The pair distribution functions show that the structural correlation in the liquid is mainly short range and that the Si-O bond is stiff. The densification of the melt structure with pressure above 50 GPa is therefore due to an increase in seven- and eightfold coordinated silicon.

DOI: [10.1103/PhysRevB.109.024106](https://doi.org/10.1103/PhysRevB.109.024106)**I. INTRODUCTION**

Silica is a reference inorganic material with a wide range of applications in the chemical industry and one of the main components in terrestrial planets' crust and interior. In spite of its chemical simplicity, the SiO<sub>2</sub> phase diagram is surprisingly rich, and a number of experimental and computational studies have attempted to draw subsolidus phase relations and melting curves to very high pressures consistent with those in the Earth's deep interior [1–7] and beyond [8–10]. Not only are these phase relations important for understanding the solid Earth's evolution from a very early stage following magma ocean crystallization, but constraining the SiO<sub>2</sub> melting curve to very high or even ultrahigh pressure may provide insight into the formation of other rocky planets such as many super-Earths. Indeed, since MgSiO<sub>3</sub> melt decomposes into SiO<sub>2</sub> and MgO at pressures above 300 GPa [11], liquid SiO<sub>2</sub> may be the most abundant phase in some of these large, rocky planets' deep interiors. High-pressure silica melting also plays an important role in the Earth's core dynamics since it has been suggested that silica may have crystallized from a Si-saturated protocore during a chemical exchange with a basal magma ocean [12,13].

Although silica phase relations have undergone several revisions experimentally and computationally, its melting curve remains poorly constrained, particularly at very high pressures consistent with those in the Earth's core and beyond, for which experimental reports are scarce. A recent shock experiment study by Millot *et al.* [8] reported a melting curve of  $T_m(P) = 1968.5 + 307.8P^{0.485}$  up to  $\sim 500$  GPa, suggesting that silica melts at around 5000 and 7000 K at pressures of the core-mantle boundary (CMB) and the Earth's inner core, respectively.

More recently, a diamond anvil cell (DAC) study by Andrault *et al.* [14,15] reported melting points up to about 150 GPa. Their melting temperatures were markedly higher ( $\approx 6000$  K at CMB pressure) than those of Millot *et al.* [8], and a very steep and abrupt change in the Clapeyron slope at  $\sim 120$  GPa was inconsistent with that seen in Ref. [8]. Two solid-liquid coexisting (two-phase) molecular dynamics simulations using classical interatomic potentials [16] and density functional theory (DFT) [1] both reported even higher melting temperatures (up to around 160 GPa) than those from the DAC experiment study, but none of these studies found any rapid change in the Clapeyron slope around 120 GPa. Moreover, a recent computational study [9,10] using the Z method together with density functional theory reported a melting curve to ultrahigh pressure ( $\sim 6000$  GPa) consistent with those in the core of gas giants and massive super-Earths (where SiO<sub>2</sub> may be the main component). Although their melting curve is in line with previous computational work up to around 150 GPa, the curve flattens markedly at around 200 GPa and is nearly flat until 300 GPa, where it abruptly climbs steeply to almost 9000 K at 400 GPa. By contrast, the experimental study by Millot *et al.* [8] did not capture any such anomalies. Clearly, there are many outstanding inconsistencies in the reported silica melting temperatures at high pressure.

Changes in the topography of the SiO<sub>2</sub> melting curve are tightly linked to any abrupt changes in the solid density and liquid structure with pressure. For example, the rapid increase in the melting curve of SiO<sub>2</sub> at a pressure of  $\sim 14$  GPa is attributable to a first-order phase transition from coesite to stishovite and involves a change in the Si coordination environment from SiO<sub>4</sub> tetrahedra to SiO<sub>6</sub> octahedra accompanied by a huge increase in density of nearly 30% [17]. Phases transitions to higher-pressure polymorphs such as  $\beta$ -stishovite (CaCl<sub>2</sub> type), seifertite ( $\alpha$ -PbO<sub>2</sub> type), and pyrite are all

\*chrism@kjemi.uio.no

accompanied by much smaller density changes of only a few percent [2,18–20]. These phase transitions are therefore not expected to impact the topography of the melting curve to an extent similar to the coesite to stishovite transition. Likewise, the distribution of coordination numbers in the liquid is intimately connected to changes in the liquid density and entropy with pressure. As the distribution of different coordination polyhedra changes along with pressure, the liquid density and entropy will change too. Understanding melting processes thus requires atomistic insight into the local structure of both solid and liquid phases at equilibrium.

Here we report results from a study of the melting curve of silica up to 500 GPa using *ab initio* density functional theory together with three methods complementary to melting: the solid-liquid coexistence method, thermodynamic integration (TI), and the Z method (together with a waiting time analysis). The influence of local structure on melting is investigated to better understand the topography of the SiO<sub>2</sub> melting curve.

## II. METHODS

### A. Two-phase coexistence method

The solid-liquid (two-phase) coexisting approach aims to target the melting temperature by equilibrating a system in which both a liquid and a solid are in mechanical contact in the simulation box. We launch *ab initio* Born-Oppenheimer molecular dynamics (BOMD) runs from an initial configuration of atoms consisting of a solid part and a liquid part with the temperature and volume kept fixed. As the system equilibrates, the fraction of the phases change along with the total pressure. If the initial pressure is higher than the equilibrium melting pressure, with  $\rho_{\text{solid}} > \rho_{\text{liquid}}$ , where  $\rho_{\text{solid}}$  and  $\rho_{\text{liquid}}$  are the average solid and liquid densities, respectively, the solid-liquid interface adjusts to increase the fraction of liquid during equilibration, thereby increasing the pressure in the direction of the equilibrium melting pressure. If the MD run is launched with a pressure that is lower than the melting pressure, the solid fraction of the box increases, and the pressure decreases toward the melting curve during equilibration. As the system propagates, the pressure fluctuates around a fixed value, the melting pressure, and the boundaries separating the solid and liquid phases do not drift. Under certain conditions, the system may melt or freeze quickly in a single simulation even with fairly large simulation boxes. However, we can still bracket the melting curve from a series of calculations at a given  $(T, P)$  and estimate the melting temperature from a statistical distribution of the number of calculations that end up as a liquid or solid [21]. When, for example, half of the calculations at a given  $(T, P)$  end up in a liquid state, the simulation temperature is the melting temperature [21,22]. Here we use a slightly different approach in which a sequence of MD runs is carried out at a given temperature with different volumes chosen to lie close to the expected liquid band. The melting pressure is then estimated from the midpoint between the MD run with the lowest pressure that froze and the MD run with the highest pressure that melted.

### B. Thermodynamic integration

From the definition of melting equilibrium, the free energies of a liquid and a solid are equal at the melting point. We

use thermodynamic integration to calculate the free energy of the liquid and solid states from an energy relationship between a reference state and an objective system,

$$F_{\text{obj}} - F_{\text{ref}} = \int_0^1 \langle U_{\text{obj}}(R) - U_{\text{ref}}(R) \rangle_{\lambda} d\lambda. \quad (1)$$

A carefully chosen sample of  $\langle U(\lambda) \rangle_{\lambda}$  calculated using *ab initio* BOMD simulations enables us to accurately calculate the free energy of the objective system with sufficient accuracy.

An ideal gas is used as the reference state in order to calculate the free energy of liquid silica:

$$F_{\text{ref}} = F_{\text{ideal gas}} = -k_{\text{B}} T \ln \frac{V^N}{\Lambda^{3N} N!}, \quad (2)$$

where  $\Lambda$  is the thermal de Broglie wavelength:

$$\Lambda = \frac{h}{\sqrt{2\pi m k_{\text{B}} T}}. \quad (3)$$

As discussed in previous studies (see, e.g., Refs. [23–25]), accurately calculating  $\langle U(\lambda) \rangle_{\lambda}$  requires a large number of  $\lambda$  points, particularly in the region where  $\lambda \rightarrow 0$  (where the ensemble is ideal-gas-like). Instead of integration over  $\lambda \in [0, 1]$ , the integration is performed over  $x \in [-1, 1]$  using

$$\lambda(x) = \left( \frac{x+1}{2} \right)^{\frac{1}{1-k}}, \quad (4)$$

where we choose  $k = 0.8$ .

The  $x$  points are chosen using a Gauss-Lobatto quadrature which is shown to give a good balance between accuracy and computational cost.

For solids, our reference state is the free energy calculated within the quasiharmonic approximation (QHA). That is,

$$F_{\text{ref}} = E_{0\text{K}} + F_{\text{har}}, \quad (5)$$

where  $E_{0\text{K}}$  is the energy of the relaxed crystal plus contributions from zero-point vibrations. The quasiharmonic vibrational term can be expressed using the phonon density of states as follows:

$$F_{\text{har}}(T) = \frac{1}{2} \sum_{qj} h\omega_{qj} + k_{\text{B}} T \sum_{qj} \ln[1 - \exp(-h\omega_{qj})/k_{\text{B}} T], \quad (6)$$

where  $q$  is the wave vector,  $j$  is the band index, and  $\omega_{qj}$  is the phonon frequency of the phonon mode labeled by a set  $\{q, j\}$ . The phonon calculations are conducted using the finite-displacement method as implemented in the PHONOPY code [26]. Thermodynamic integration is then used to calculate the anharmonic contribution to the solid from Eq. (1) using the Gauss-Legendre quadrature to integrate over  $x \in [-1, 1]$  by the changes in variables from  $\lambda \in [0, 1]$  using

$$\lambda(x) = \frac{x+1}{2}. \quad (7)$$

Since the reference state is the “static state” plus QHA corrections for the solid [Eq. (5)], the difference between the reference and object functions reflects mainly the anharmonic contribution to the free energy.

### C. Z method

The Z method calculates the melting temperature from the relationship between a material’s homogeneous melting temperature (superheating limit) and its equilibrium melting temperature [16,27,28]. A sequence of molecular dynamics simulations is launched in the *NVE* ensemble [29] at different initial temperatures  $T_{\text{ini}}$  to target the lowest total energy  $E_h$  (and highest temperature  $T_h$ ) where the solid melts. The maximum energy along the solid branch of the isochore is the same as the lowest energy along the liquid branch,

$$E^{\text{sol}}(V, T_h) = E^{\text{liq}}(V, T_m). \quad (8)$$

When the system melts at  $T_h$ , the temperature decreases to a distinct value,  $T_m$ , the equilibrium melting temperature, while the latent heat of melting is gradually converted to potential energy. The relationship between  $T_h$  and  $T_m$  is given by [27,30]

$$\frac{T_h}{T_m} - 1 = \frac{\Delta S_m}{C_V}. \quad (9)$$

Here  $C_V$  is the heat capacity of the solid, and  $\Delta S_m$  is the melting entropy.

Since the waiting time for the solid to melt diverges when  $T$  tends to  $T_h$ , the calculated melting temperature will always, in theory, represent an upper bound to the “true” melting temperature. To avoid extremely long MD runs in the vicinity of  $T_h$ , the melting temperature is instead often calculated from an extrapolation of the distributions of waiting times from a sequence of runs with  $E = (E_h + \Delta E)$  using

$$\langle \tau \rangle^{-1/2} = A(T_{\text{liq}} - T_m), \quad (10)$$

where  $A$  is a parameter,  $\tau$  is the waiting time for a given total energy, and  $T_{\text{liq}}$  is the temperature of the system after melting [28]. When  $\Delta E \rightarrow 0$ ,  $T_{\text{liq}} \rightarrow T_m$ , and the melting temperature is found at the point of intersection where  $\langle \tau \rangle^{-1/2} = 0$ .

Implementation of the Z method together with DFT typically uses *ab initio* BOMD in the *NVE* ensemble, in which the Fermi-Dirac electronic temperature is kept fixed along the entire trajectory. Although this ensures conserved dynamics using the Hellmann-Feynman forces to propagate the ions [31,32], large changes in the temperature following melting and equilibration may introduce systematic errors in the calculated melting temperature. The difference in melting temperature when  $T_{\text{el}} \approx T_h$  and  $T_{\text{el}} \approx T_m$ , representing reasonable lower and upper bounds to  $T_m$ , respectively, is about 200 K for  $\text{SiO}_2$  at around 160 GPa and 6000 K [33]. Here we choose an electronic entropy close to the predicted melting temperature. Although this ensures a correct ion-electron interaction in the liquid state of the MD simulation, the electronic temperature is slightly too low before melting, and the melting temperature will probably be overestimated by  $\sim 100$  K [33].

### III. COMPUTATIONAL DETAILS

All calculations carried out in this work were performed using the Vienna Ab initio Simulation Package (VASP) [34,35] together with the generalized gradient approximation (GGA) functional (parametrized using the Perdew-Burke-Ernzerhof scheme) [29] to calculate the exchange-correlation contribution to the total energy implemented with projector

augmented waves [36,37]. The valence electron configurations were  $2s^2p^4$  for O and  $3s^23p^2$  for Si with core radii of 1.95 and 1.55 Å, respectively, for the projector operator. Two-phase test calculations of thermodynamic (average pressure) and structural properties [pair distribution functions (PDFs)] carried out using the “hard” oxygen potential (with a core radius of 1.228 Å) were in excellent agreement with those calculated using the default potentials. For example, the average pressure for pyrite at 8000 K with hard O potentials was within the error bars of that reported using default potentials, and the PDFs were nearly indistinguishable.

A cutoff energy of 400 eV for the plane waves was used in the two-phase simulations. Test calculations carried out using a cutoff energy of 500 eV gave ensemble average properties (i.e., average pressures and PDFs) within the error bars reported using a 400 eV energy cutoff. Since a markedly smaller cell size was used in the Z method calculations compared to the two-phase calculations, the energy cutoff was slightly higher (700 eV). In the TI calculations, we analyzed the convergence of the static energy from a sequence of runs from 500 to 1000 eV. We found that the total energy was sufficiently converged ( $<0.001$  eV/atom) using an energy cutoff of 800 eV. This value is used for all the calculations carried out in the static limit as well as in the QHA runs;  $4 \times 4 \times 4$  supercells are used in the evaluation of the harmonic vibrational contribution to the total free energy. In the MD simulations in which the anharmonic contribution to the solid free energy was calculated, we found that an energy cutoff of 500 eV was sufficient. That is, we found that the DFT energies calculated from MD runs with a higher energy cutoff of 800 eV differ by only about 0.00103 eV/atom compared to that calculated using an energy cutoff of 500 eV. Only the  $\Gamma$  points were used in all the MD runs used in the two-phase, TI, and Z method calculations, whereas a  $4 \times 4 \times 4$  Monkhorst-Pack mesh was used in the TI calculations for the solid carried out in the static limit.

In all *NVT* MD runs the electronic entropy was included using a Fermi-Dirac smearing scheme with a width of  $k_B T$  [31]. As discussed above, special attention was given to the choice of electronic temperature in the Z method calculations because of the large temperature drop that accompanied melting in the simulations. We evaluated the melting temperatures using three different electronic temperatures ranging from 5500 to 7500 K for seifertite and 6000 to 8000 K for pyrite. The electronic temperature which is closest to  $T_m$  is chosen in the waiting time analysis, and the values used are reported in the Supplemental Material (SM) [38].

The molecular dynamics runs used in the two-phase calculations and the TI free energy calculations were carried out using a Nosé-Hoover thermostat with a time step of 1 fs (TI) or 2 fs. A smaller time step of 0.5 fs was used in the Z method calculations.

For the liquid TI simulations,  $\langle U(\lambda) \rangle_\lambda$  was evaluated with an integration of 8  $\lambda$  points using a Gauss-Lobatto quadrature. The energy difference between 8  $\lambda$  points and 10  $\lambda$  points evaluated in a 162-atom simulation box is only  $\sim 0.0008$  eV/atom, suggesting that 8  $\lambda$  points is sufficient (see the SM, Table S2 and Fig. S1, where we plot the convergence of the free energy with the number of  $\lambda$  points).

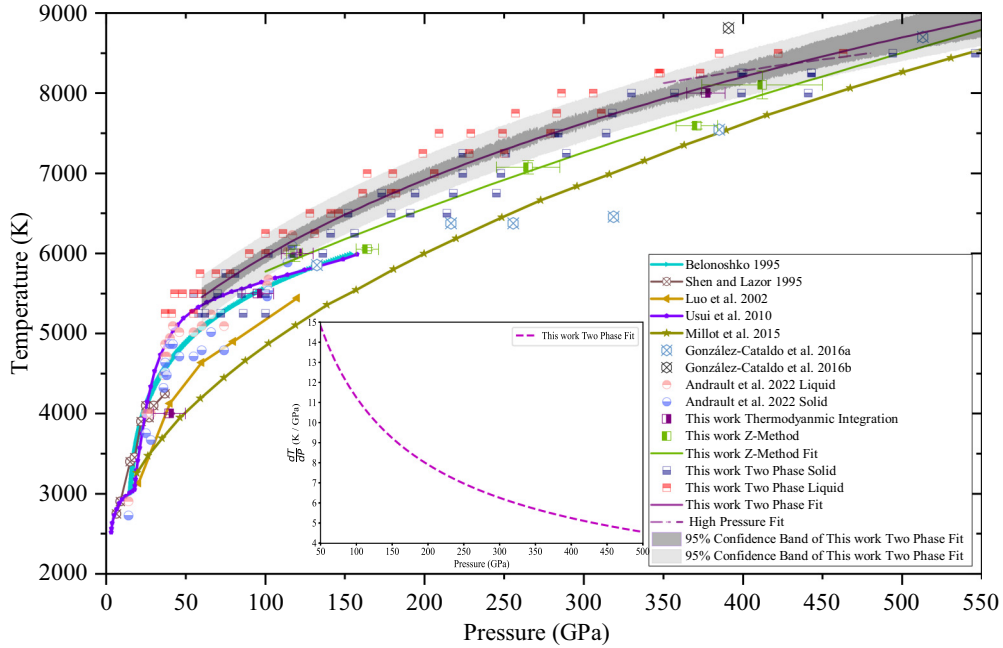


FIG. 1. Melting points and melting curves of SiO<sub>2</sub> from this work and the literature. We fitted Simon-Glatzel melting equations using  $T_{\text{melting}}(P) = T_0 \times (1 + \frac{P-P_0}{a})^b$  to the melting points from the Z method and two-phase calculations, which gave the following parameters:  $T_0 = 6.018$ ,  $P_0 = -202.338$ ,  $a = 4.736 \times 10^{-4}$ , and  $b = 0.5126$  (two-phase calculations) and  $T_0 = 6.462$ ,  $P_0 = -256.011$ ,  $a = 6.474 \times 10^{-4}$ , and  $b = 0.5141$  (Z method calculations). For the two-phase calculations the data points used in the fitting were the mean values of the lowest liquid and highest solid phases at a given temperature. All data points from the two-phase calculations are also reported in Table S1 in the SM. The inset shows the steepness of the melting curves from the two-phase coexistence calculations.

The two-phase coexistence calculations were carried out using a 486-atom simulation cell for stishovite and  $\beta$ -stishovite, whereas a 648-atom cell was used for seifertite and pyrite. These simulation boxes are made from units constructed from the primitive SiO<sub>2</sub> unit cell of a given solid phase. The liquid portion of the two-phase simulation box was constructed by first heating to above the homogeneous melting temperature, followed by a decrease in temperature to  $T_{\text{ini}}$ . The solid portion was then heated until  $T_{\text{ini}}$ , and two equal volumes of the solid and liquid subunits were glued together [22]. We then launched the two-phase MD simulations at  $T_{\text{ini}}$  following the procedure discussed in the Sec. II Methods. All two-phase calculations ran for at least 5 ps and sometimes for more than 40 ps before they froze or melted. After they fully melted (or crystallized) the MD runs continued for at least 1 ps to calculate the equilibrium pressure with sufficient accuracy. Equilibrium pressures and relaxation times for melting or freezing are reported in Table S1.

We also investigated the sensitivity to melting using different surface cutoff schemes to represent the solid-liquid phase boundary. A comparison with calculations carried out on stishovite using a (001) vs a (100) crystallographic cutoff plane showed very similar melting temperatures.

In total, we carried out more than 100 two-phase calculations in the pressure range from 50 to 500 GPa, and details for most of these (including those used in the calculation of the melting curve) are reported in Table S1 in the SM. We used a large pressure overlap ( $\sim 25$  GPa) for the different solid phases to ensure that the correct (equilibrium) solid phases were used to calculate the melting curve. The expected stability range of the solids was estimated from an extrapolation of the

Clapeyron slopes determined from recent computational and experimental studies (see, e.g., [2] and references therein).

#### IV. RESULTS AND DISCUSSION

In Fig. 1 we collect calculated melting temperatures using the Z method, TI, and two-phase method together with previously reported results in the literature. We focus here on the functional form of the SiO<sub>2</sub> liquidus above about 50 GPa because the steep increase in the melting curve between 14 and 50 GPa due to the coesite-stishovite transitions is well documented [39–44]. Above about 50 GPa our melting curves flatten significantly, and the discrepancy between the different melting temperatures and curves reported in the literature spans more than 1000 K in a large pressure interval. The Z method and two-phase melting curves are in very good agreement overall with the melting points calculated using TI at around 100, 120, and 377 GPa, but the calculated TI melting temperature at around 50 GPa is somewhat lower compared to the melting curve from our two-phase and Z method calculations as well as previous computational work [1,9]. This discrepancy may be due to the possibly large error bars in the solid and liquid free energy curves using TI and the extremely steep melting curve below 50 GPa.

The melting curve from the two-phase calculations have a  $dT/dP \approx 14$  K/GPa at around 50 GPa, and the  $dT/dP$  is about 5 K/GPa at 500 GPa without any abrupt changes in the functional form. A possible flattening anomaly above about 300 GPa is indicated in Fig. 1 as a dashed line. Such a small anomaly could possibly be due to an increase in the liquid electronic entropy rather than the configurational liquid

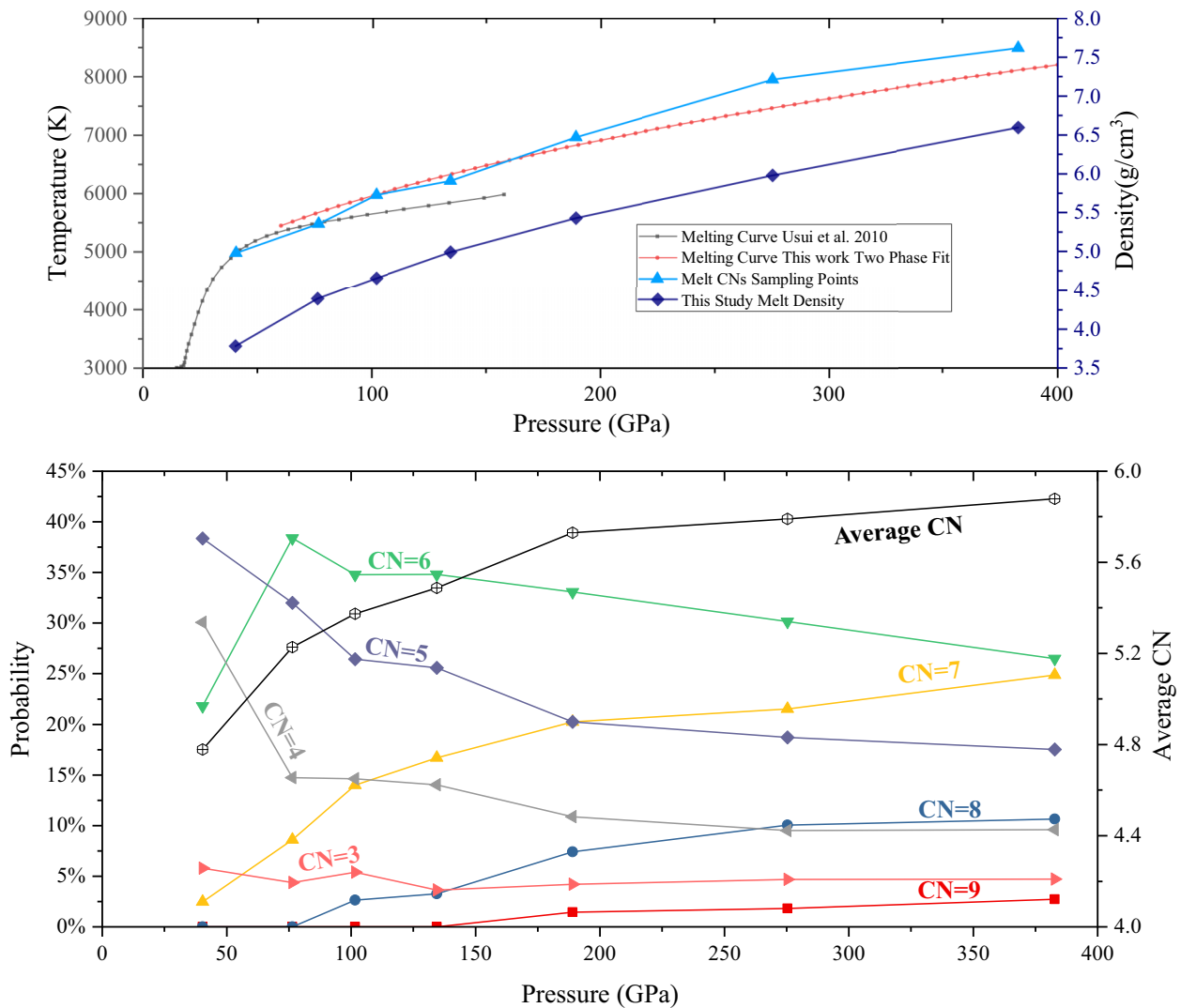


FIG. 2. Top and bottom graphs show the changes in the density and Si coordination numbers, respectively, in liquid SiO<sub>2</sub> near the melting curve. The coordination numbers are evaluated with a near-neighbor algorithm [48] which uses a Voronoi decomposition scheme to determine the probability of various coordination numbers and then select the one with the highest probability.

entropy since there are no changes in the liquid structure (i.e., distribution of coordination numbers) that point to a configurational stabilization of the liquid state above 200 GPa. That is, in a large pressure interval from 200 to 400 GPa, the average coordination number (CN) for Si increases by less than 0.2 from 5.7 to 5.9 (Fig. 2).

Although the Z method and two-phase melting curves are in good agreement overall in the entire pressure range studied, the Z method curve is slightly lower by about 300 K, and the Simon-Glatzel fit to the Z method data indicates a slightly flatter curve at lower pressures compared with the two-phase melting curve. Since the same parameters for the electronic wave function were used in the two methods, a possible explanation for the small discrepancy could be the statistics, cell size effects, or choice of electronic entropy in the *NVE* MD runs (Z method).

In particular, the choice of electronic entropy is not evident in MD runs carried out in the *NVE* ensemble because the Mermin free energy plus the ionic kinetic energy is a conserved quantity, with the forces being propagated using

Hellmann-Feynman dynamics [32]. This means that the electronic temperature  $T_{el}$  is kept fixed along the entire trajectory. A fixed electronic temperature, however, may introduce errors in the calculated melting temperature because it is unable to correctly capture electron-ion dynamics in both the solid and liquid portions of the MD simulation since the temperature difference between these states is large. If an MD run is launched in the *NVE* ensemble with  $T_{el}$  chosen to be near the liquid temperature, then  $T_{el}$  will be much lower than the ensemble temperature in the solid state (before melting). A too low electronic entropy, however, may favor the stabilization of the solid and prevent melting. This will affect the estimated homogeneous melting temperature and also the “waiting time” for a solid to melt. Thus, the calculated melting temperature may be too high. If an MD run is launched with a much higher electronic temperature, for example, chosen to lie close to the temperature of the solid state, a physically reasonable electronic-ionic interaction is ensured only before melting. This is because once the solid melts at a constant volume and total energy, the temperature drops by

$(1 - T_m/T_h)T_m \approx 2000$  K (see Fig. S6), and the electronic entropy will be much *higher* than the liquid temperature [33]. This generally favors an entropic stabilization of the liquid, and the melting temperature may be too low. Here we choose  $T_{el} \approx T_m$  in the Z method calculations, indicating that the melting temperature may be slightly overestimated by about 100 K for SiO<sub>2</sub> at  $T \sim 6000$  K [33] (see also Fig. S6 in the SM). Other possible sources of the small discrepancy between these two curves could be the formation of defects in the solid state accompanying freezing. Such defects were not seen in the Z method runs when the box melted homogeneously, but we noted that such defects sometimes form in the two-phase calculations (as marked in Table S1 in the SM). Anyhow, the overall good agreement between all three methods employed in this work is encouraging and suggests the melting curve is well represented by the smooth Simon-Glatzel fits shown in Fig. 1.

The good agreement between our melting curves and that reported by Usui and Tsuchiya [1] (plotted in Fig. 1) is therefore possibly fortuitous because a very small two-phase simulation box containing only 96 atoms was used in Ref. [1]. Such a box has a boundary similar in size to (or larger than) the solid and liquid portions of the simulation box, and extensive statistics is needed to precisely determine the melting temperature using such a small two-phase cell [21,22]. Moreover, the slope in Ref. [1] above about 60 GPa is also markedly less steep than our melting curves, suggesting that it will lie markedly lower than that of Millot *et al.* [8] if extrapolated above 200 GPa.

It is also worth noting that our results are inconsistent with the Z method calculations reported by González-Cataldo *et al.* [9,10]. Whereas our curves show a smooth increase in the pressure region between 200 and 400 GPa, the melting points of González-Cataldo *et al.* [9,10] indicate a nearly flat curvature from 200 to 350 GPa, followed by an abrupt increase in temperature by more than 2500 K at around 400 GPa. This anomaly was explained in Ref. [9] by the seifertite to pyrite transition, which has been suggested to take place at around 280 GPa according to an experimental high-pressure study [18]. Computational studies, however, consistently show that this transition takes place at a much lower pressure, i.e., at around 200 GPa or slightly less [2,7]. For example, highly accurate hybrid functionals of DFT together with lattice dynamics predict that the transition to pyrite takes place at around 200 GPa [2], indicating that the experimental work by Kuwayama *et al.* [18] may be poorly constrained. Indeed, the outcomes of four different experiments reported in Ref. [18] all indicate a nearly vertical, but weakly constrained,  $dP/dT$  slope, and the low experimental temperatures ( $<2000$  K) could therefore explain the delay in the transition pressure due to slow kinetics. Such a “delayed” phase transition has also been observed for other phase transitions in silica, for example, the  $\beta$ -stishovite to seifertite transition (see, e.g., Ref. [5]), resulting in a too high transition pressure before the high-pressure phase is visible in the x-ray diffraction patterns.

Moreover, the volume drop accompanying the seifertite to pyrite transition is expected to be around 4% [2,18], which is probably too small to explain the rapid increase in the melting curve close to 400 GPa, as suggested in Refs. [9,10]. An explanation for such a steep slope can possibly be associated

with the choice of electronic temperature in the DFT calculations and/or slow equilibration in the MD *NVE* runs close to the homogeneous melting temperature which may prevent melting. To investigate the origin of the discrepancy between our melting curves and the melting point reported in Ref. [10] at 8826 K and 391 GPa using the Z method, we attempted to reproduce their high-temperature melting anomaly. We thus carried out MD simulations with an initial temperature of 25 000 K and  $T_{el} = 7500$  K with all atoms initially located at their equilibrium positions. This initial temperature is slightly lower than that used in Ref. [10], which is 26 000 K. With these parameters, pyrite melts quickly ( $<5$  ps in all our 11 parallel MD runs), reaching an average liquid temperature and pressures of 8608 K and 383 GPa. This is quite close to the liquid point estimated in Ref. [10] (i.e., 391 GPa and 8826 K). Although no electronic temperatures were reported in Ref. [10], reasonable choices in the range 6000–9000 K are expected to influence the melting temperature to less than 300 K [33]. Rapid melting in our MD simulations with  $T_{ini} = 25000$  K, however, indicate that the liquid temperature with this choice of initial conditions is far higher than the equilibrium melting temperatures. When we decrease the initial temperature to as low as 22 000 K, the system still melts, but the waiting time before melting is more than 120 ps in all 11 parallel MD runs, and the liquid temperature is 7747 K at 372 GPa. This is only about 100 K higher than the equilibrium melting temperature extracted from a waiting time analysis. This confirms that liquid temperature in MD runs with  $T_{ini} = 26000$  K [10], assuming that the atoms are initially distributed over their ideal positions with a reasonable choice of  $T_{el}$ , is  $\approx 1000$  K higher than the equilibrium melting temperature at 390 GPa.

Our MD simulations may also provide insight into the kinetics of shock-compressed silica and shed some light on the discrepancy between our SiO<sub>2</sub> equilibrium melting curve and that extracted from the shock experiment by Millot *et al.* [8]. Shock Hugoniot appear to lie at different branches corresponding to amorphous or crystalline states depending on experimental methodologies and timescales [45]. If the liquid is unable to relax to the crystalline state at the timescale of the shock pressure, one might expect that the Hugoniot may lie at lower temperatures compared to that of a fully relaxed (crystalline) state. Indeed, large-scale atomistic MD simulations carried out by Shen *et al.* [45] show that points on the amorphous Hugoniot will shift to the crystallized branch at longer timescales. The discrepancy between our equilibrium melting curve and that predicted from a shock study by Millot *et al.* [8] could therefore be due to the incomplete crystallization of stishovite or amorphous shock-compressed silica.

Changes in density and coordination numbers with pressure are shown in Fig. 2 and the total and partial PDFs in Fig. 3. The Si-O PDF shows that the correlation length in the liquid state is mainly short range ( $<5$  Å), pointing to a high liquid entropy quantified by the relative distribution of Si CNs. (see bottom Fig. 2). Comparison of the Si-O partial PDFs at different pressures along the liquidus shows surprisingly small changes in the Si-O bond length: The first peak in the Si-O partial PDF is located at 1.65 Å at 6000 K and 100 GPa, whereas Si-O bonds are only about 0.1 Å shorter at 8250 K and 373 GPa. The driving force to increasing liquid

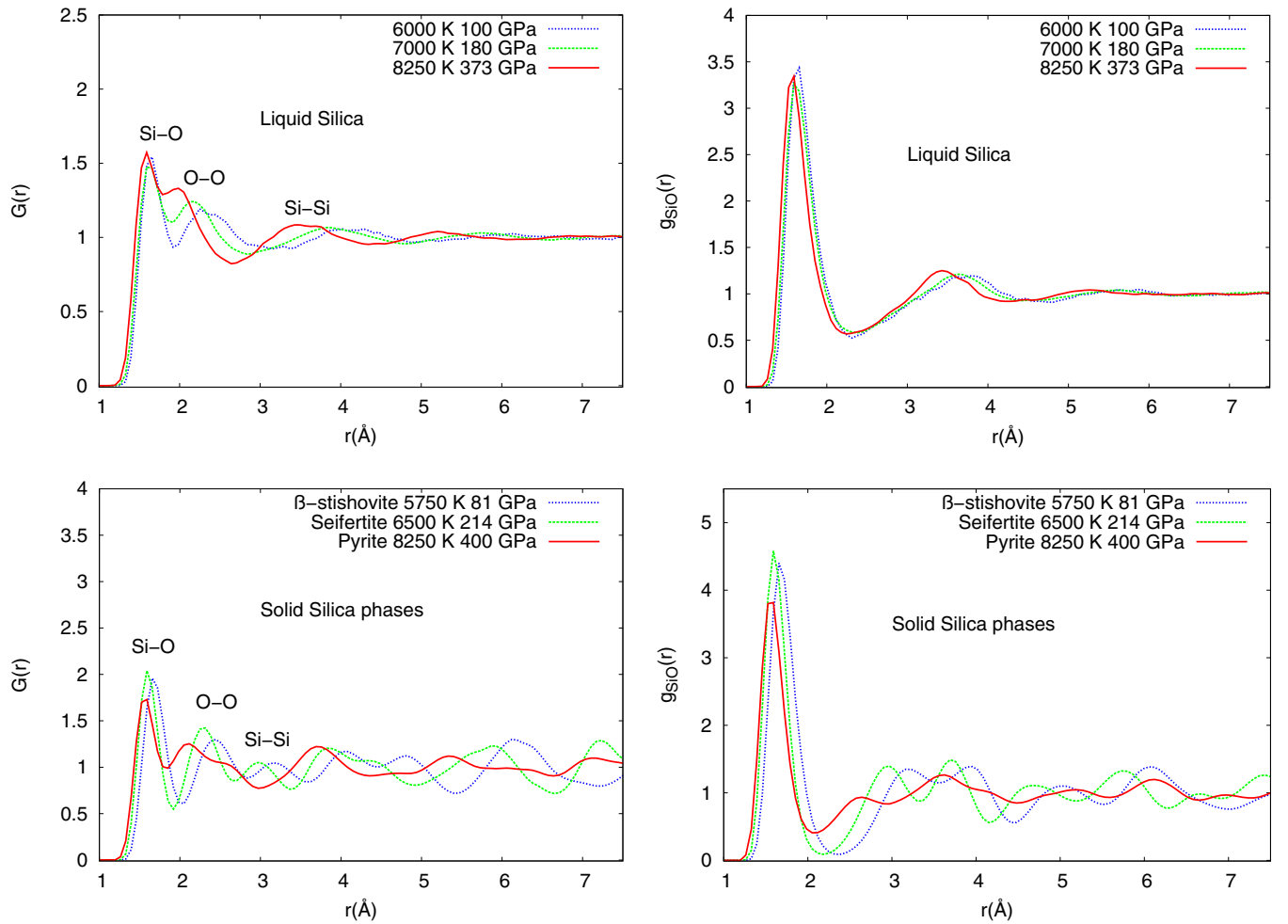


FIG. 3. Top left and right plots show the total and partial (Si-O) PDFs for liquid silica, whereas the bottom left and right plots show the corresponding (total and partial) PDFs for the solid phases.

density (and entropy) is therefore due to changes in local coordination and/or electronic entropy. In particular, the electronic entropy could be the main source of the very flat melting curve above 300 GPa since there is very little change in the liquid structure in this region, reflected by a very small increase in the average Si CN from 5.8 (300 GPa) to 5.9 (400 GPa) with pressure (Fig. 2).

The partial PDFs of the solids are in good agreement with previous studies overall (see, e.g., Ref. [6]). For example, the comparison of the nearest-neighbor O-O distances is at about 2.2 Å at 214 GPa, in good agreement with that seen in Ref. [6] at slightly lower pressure. In Fig. S7 in the SM, we collect x-ray diffraction patterns of the liquid at two pressures (76 and 275 GPa). The pattern is consistent with the that of a previous study [46,47] containing a broad peak that shifts to higher values of  $2\theta$  with increasing pressure, in line with the increasing densification of liquid with short-range correlation.

## V. CONCLUSIONS

We have constrained the melting curve of pure silica from about 50 to 500 GPa using DFT at the level of GGA together with three complementary approaches to melting: the solid-

liquid coexistence approach, thermodynamic integration, and the Z method. The melting curves/points from the three different approaches are in very good agreement overall. After an abrupt increase following the transition to stishovite, the two-phase melting curves flatten markedly at about 50 GPa and increase smoothly from about 50 GPa with a  $dT/dP$  slope of  $\approx 15$  K/GPa to about 500 GPa with  $dT/dP \approx 5$  K/GPa. We do not see any evidence of the abrupt change at around 120 GPa which was seen in a recent experimental study [14,15] or the flattening at 200 GPa followed by an abrupt increase of almost 1500 K in the pressure window from 300 to 400 GPa as observed from simulations using the Z method reported in Ref. [9]. The topography of the melting curves from 50 to 500 GPa is consistent with a gradual change in the distribution of the Si coordination numbers in the liquid state and the absence of large changes in the density following solid-solid phase transitions. The pair distribution functions show that the correlations in the liquid structure are mainly short range and that the Si-O bond decreases by less than 0.2 Å along the melting line from 100 to 400 GPa. The densification of the melt structure with pressure above 50 GPa is therefore mainly due to a gradual increase in seven-, eight-, and ninefold coordinated silicon and a gradual decrease in Si with six or fewer oxygens in the first coordination shell.

## ACKNOWLEDGMENTS

We thank J.-A. Hernandez for useful input on the manuscript. We acknowledge financial support from the Research Council of Norway through its Centres of

Excellence scheme, Project No. 223272 (CEED) and Project No. 332523 (PHAB). Computational resources were provided by the Norwegian infrastructure for high-performance computing (NOTUR, Sigma-2, Grants No. NN9329K and No. NN2916K).

- [1] Y. Usui and T. Tsuchiya, Ab initio two-phase molecular dynamics on the melting curve of SiO<sub>2</sub>, *J. Earth Sci.* **21**, 801 (2010).
- [2] P. K. Das, C. E. Mohn, J. P. Brodholt, and R. G. Trønnes, High-pressure silica phase transitions: Implications for deep mantle dynamics and silica crystallization in the protocore, *Am. Mineral.* **105**, 1014 (2020).
- [3] J. A. Akins and T. J. Ahrens, Dynamic compression of SiO<sub>2</sub>: A new interpretation, *Geophys. Res. Lett.* **29**, 31 (2002).
- [4] B. Grocholski, S.-H. Shim, and V. B. Prakapenka, Stability, metastability, and elastic properties of a dense silica polymorph, seifertite, *J. Geophys. Res.: Solid Earth* **118**, 4745 (2013).
- [5] M. Murakami, K. Hirose, S. Ono, and Y. Ohishi, Stability of CaCl<sub>2</sub>-type and  $\alpha$ -PbO<sub>2</sub>-type SiO<sub>2</sub> at high pressure and temperature determined by in-situ x-ray measurements, *Geophys. Res. Lett.* **30**, 1207 (2003).
- [6] Y. Kuwayama, K. Hirose, N. Sata, and Y. Ohishi, Pressure-induced structural evolution of pyrite-type SiO<sub>2</sub>, *Phys. Chem. Miner.* **38**, 591 (2011).
- [7] A. R. Oganov, M. J. Gillan, and G. D. Price, Structural stability of silica at high pressures and temperatures, *Phys. Rev. B* **71**, 064104 (2005).
- [8] M. Millot, N. Dubrovinskaia, A. Černok, S. Blaha, L. Dubrovinsky, D. G. Braun, P. M. Celliers, G. W. Collins, J. H. Eggert, and R. Jeanloz, Shock compression of stishovite and melting of silica at planetary interior conditions, *Science* **347**, 418 (2015).
- [9] F. González-Cataldo, S. Davis, and G. Gutiérrez, Melting curve of SiO<sub>2</sub> at multimegabar pressures: Implications for gas giants and super-Earths, *Sci. Rep.* **6**, 26537 (2016).
- [10] F. González-Cataldo, S. Davis, and G. Gutiérrez, Z method calculations to determine the melting curve of silica at high pressures, *J. Phys.: Conf. Ser.* **720**, 012032 (2016).
- [11] B. Boates and S. A. Bonev, Demixing instability in dense molten MgSiO<sub>3</sub> and the phase diagram of MgO, *Phys. Rev. Lett.* **110**, 135504 (2013).
- [12] K. Hirose, Crystallization of silicon dioxide and compositional evolution of the Earth's core, *Nature (London)* **543**, 99 (2017).
- [13] R. G. Trønnes, M. A. Baron, K. R. Eigenmann, M. G. Guren, B. H. Heyn, A. Løken, and C. E. Mohn, Core formation, mantle differentiation and core-mantle interaction within Earth and the terrestrial planets, *Tectonophysics* **760**, 165 (2019).
- [14] D. Andrault, L. Pison, G. Morard, G. Garbarino, M. Mezouar, M. A. Bouhifd, and T. Kawamoto, Comment on: Melting behavior of SiO<sub>2</sub> up to 120 GPa (Andrault et al 2020), *Phys. Chem. Miner.* **49**, 3 (2022).
- [15] D. Andrault, G. Morard, G. Garbarino, M. Mezouar, M. A. Bouhifd, and T. Kawamoto, Melting behavior of SiO<sub>2</sub> up to 120 GPa, *Phys. Chem. Miner.* **47**, 10 (2020).
- [16] A. B. Belonoshko and L. S. Dubrovinsky, Molecular dynamics of stishovite melting, *Geochim. Cosmochim. Acta* **59**, 1883 (1995).
- [17] M. Akaogi, M. Oohata, H. Kojitani, and H. Kawaji, Thermodynamic properties of stishovite by low-temperature heat capacity measurements and the coesite-stishovite transition boundary, *Am. Mineral.* **96**, 1325 (2011).
- [18] Y. Kuwayama, K. Hirose, N. Sata, and Y. Ohishi, The pyrite-type high-pressure form of silica, *Science* **309**, 923 (2005).
- [19] C. Liu, J. Shi, H. Gao, J. Wang, Y. Han, X. Lu, H.-T. Wang, D. Xing, and J. Sun, Mixed coordination silica at megabar pressure, *Phys. Rev. Lett.* **126**, 035701 (2021).
- [20] G. Li, Z. Zhang, X. Niu, J. Liu, J. Li, W. Wang, and Z. Zhang, Equations of state and phase boundaries of SiO<sub>2</sub> polymorphs under lower mantle conditions, *J. Geophys. Res.: Solid Earth* **128**, e2023JB026774 (2023).
- [21] Q.-J. Hong and A. van de Walle, A user guide for sluschi: Solid and liquid in ultra small coexistence with hovering interfaces, *CALPHAD: Comput. Coupling Phase Diagrams Thermochem.* **52**, 88 (2016).
- [22] J.-A. Hernandez, C. E. Mohn, M. G. Guren, M. A. Baron, and R. G. Trønnes, Ab initio atomistic simulations of Ca-perovskite melting, *Geophys. Res. Lett.* **49**, e2021GL097262 (2022).
- [23] F. Dorner, Z. Sukurma, C. Dellago, and G. Kresse, Melting Si: Beyond density functional theory, *Phys. Rev. Lett.* **121**, 195701 (2018).
- [24] T. Sun, J. P. Brodholt, Y. Li, and L. Vočadlo, Melting properties from *ab initio* free energy calculations: Iron at the Earth's inner-core boundary, *Phys. Rev. B* **98**, 224301 (2018).
- [25] M. Rang and G. Kresse, First-principles study of the melting temperature of MgO, *Phys. Rev. B* **99**, 184103 (2019).
- [26] A. Togo and I. Tanaka, First principles phonon calculations in materials science, *Scr. Mater.* **108**, 1 (2015).
- [27] A. B. Belonoshko, N. V. Skorodumova, A. Rosengren, and B. Johansson, Melting and critical superheating, *Phys. Rev. B* **73**, 012201 (2006).
- [28] D. Alfé, C. Cazorla, and M. J. Gillan, The kinetics of homogeneous melting beyond the limit of superheating, *J. Chem. Phys.* **135**, 024102 (2011).
- [29] J. P. Perdew, K. Burke, and M. Ernzerhof, Generalized gradient approximation made simple, *Phys. Rev. Lett.* **77**, 3865 (1996).
- [30] J. Braithwaite and L. Stixrude, Melting of CaSiO<sub>3</sub> perovskite at high pressure, *Geophys. Res. Lett.* **46**, 2037 (2019).
- [31] N. D. Mermin, Thermal properties of the inhomogeneous electron gas, *Phys. Rev.* **137**, A1441 (1965).
- [32] R. M. Wentzcovitch, J. L. Martins, and P. B. Allen, Energy versus free-energy conservation in first-principles molecular dynamics, *Phys. Rev. B* **45**, 11372 (1992).
- [33] M. Geng and C. E. Mohn, Influence of electronic entropy on Hellmann-Feynman forces in *ab initio* molecular dynamics with large temperature changes, *Phys. Rev. B* **108**, 134110 (2023).
- [34] G. Kresse and J. Hafner, *Ab initio* molecular dynamics for liquid metals, *Phys. Rev. B* **47**, 558 (1993).
- [35] G. Kresse and J. Hafner, *Ab initio* molecular-dynamics simulation of the liquid-metal-amorphous-semiconductor transition in germanium, *Phys. Rev. B* **49**, 14251 (1994).



- [36] P. E. Blöchl, Projector augmented-wave method, *Phys. Rev. B* **50**, 17953 (1994).
- [37] G. Kresse and D. Joubert, From ultrasoft pseudopotentials to the projector augmented-wave method, *Phys. Rev. B* **59**, 1758 (1999).
- [38] See Supplemental Material at <http://link.aps.org/supplemental/10.1103/PhysRevB.109.024106> for choice of parameters, detail of computational methods and convergency test of methods. Also, the structure analysis of the silica melts at high pressure.
- [39] S.-I. Akimoto and Y. Syono, Coesite-stishovite transition, *J. Geophys. Res.* **74**, 1653 (1969).
- [40] T. Yagi and S.-I. Akimoto, Direct determination of coesite-stishovite transition by in-situ x-ray measurements, *Tectonophysics* **35**, 259 (1976).
- [41] G. Serghiou, A. Zerr, L. Chudinovskikh, and R. Boehler, The coesite-stishovite transition in a laser-heated diamond cell, *Geophys. Res. Lett.* **22**, 441 (1995).
- [42] J. Zhang, B. Li, W. Utsumi, and R. C. Liebermann, In situ x-ray observations of the coesite-stishovite transition: Reversed phase boundary and kinetics, *Phys. Chem. Miner.* **23**, 1 (1996).
- [43] Q. Y. Hu, J. F. Shu, A. Cadien, Y. Meng, W. G. Yang, H. W. Sheng, and H. K. Mao, Polymorphic phase transition mechanism of compressed coesite, *Nat. Commun.* **6**, 6630 (2015).
- [44] M. Krug, M. Saki, E. Ledoux, J. P. Gay, J. Chantel, A. Pakhomova, R. Husband, A. Rohrbach, S. Klemme, C. Thomas, S. Merkel, and C. Sanchez-Valle, Textures induced by the coesite-stishovite transition and implications for the visibility of the x-discontinuity, *Geochem., Geophys., Geosyst.* **23**, e2022GC010544 (2022).
- [45] Y. Shen, S. B. Jester, T. Qi, and E. J. Reed, Nanosecond homogeneous nucleation and crystal growth in shock-compressed SiO<sub>2</sub>, *Nat. Mater.* **15**, 60 (2016).
- [46] H. Niu, P. M. Piaggi, M. Invernizzi, and M. Parrinello, Molecular dynamics simulations of liquid silica crystallization, *Proc. Natl. Acad. Sci. USA* **115**, 5348 (2018).
- [47] B. Kalkan, B. K. Godwal, J. Yan, and R. Jeanloz, High-pressure phase transitions and melt structure of PbO<sub>2</sub>: An analog for silica, *Phys. Rev. B* **105**, 064111 (2022).
- [48] N. E. R. Zimmermann and A. Jain, Local structure order parameters and site fingerprints for quantification of coordination environment and crystal structure similarity, *RSC Adv.* **10**, 6063 (2020).